

1 **Fossilization of Precambrian microfossils in the Volyn pegmatite,**
2 **Ukraine**

3
4 Gerhard Franz¹, Peter Lyckberg², Vladimir Khomenko³, Vsevolod Chournousenko⁴, Hans-
5 Martin Schulz⁵, Nicolaj Mahlstedt⁵, Richard Wirth⁵, Johannes Glodny⁵, Uli Gernert⁶, Jörg
6 Nissen⁶

7 ¹Institut für Angewandte Geowissenschaften, Technische Universität Berlin, D-10587 Berlin,
8 Germany

9 ²Luxembourg National Museum of Natural History, 25 Rue Münster, 2160 Luxembourg,
10 Luxembourg

11 ³The National Academy of Sciences of Ukraine, M.P. Semenenko Institute of Geochemistry,
12 Mineralogy and Ore Formation, 34, Palladina av., Kyiv, 03142, Ukraine

13 ⁴Volyn Quartz Samotsvety Company, Khoroshiv (Volodarsk-Volynski), Ukraine

14 ⁵GFZ German Research Centre for Geosciences, Telegrafenberg, D-14473 Potsdam, Germany

15 ⁶Zentraleinrichtung Elektronenmikroskopie, Technische Universität Berlin, D-10623 Berlin,
16 Germany

17
18

19 Corresponding author: Gerhard Franz; e-mail: gefra548@gmail.com

20 **Abstract**

21 We report on Precambrian microfossils from igneous rocks of the Volyn pegmatite district,
22 associated with the Paleoproterozoic Korosten Pluton, north-western Ukraine. The fossils were
23 recovered from m-sized miarolitic cavities and show a well-preserved 3D morphology, mostly
24 filamentous, but with a large variety of types, and also in irregular, flaky shapes reminiscent of
25 former biofilms, and rare spherical objects. Based on literature data, pyrolysis experiments and
26 reflected light microscopy results, the organic matter (OM) is characterized as (oxy)kerite.
27 Further investigations with microscopic techniques, including scanning and transmission
28 electron microscopy, and electron microprobe analysis show that fossilization likely occurred
29 during a hydrothermal, post-pegmatitic event, by silicification dominantly in the outermost 1-
30 2 μm of the microfossils. The hydrothermal fluid, derived from the pegmatitic environment,
31 was enriched in SiF_4 , Al, Ca, Na, K, Cl, and S. The OM shows O enrichment where N and S
32 content is low, indicating simultaneous N and S loss during anaerobic oxidation. Mineralization
33 with Al-silicates starts at the rim of the microfossils, continues in its outer parts into identifiable
34 encrustations and intergrowths of clay minerals, feldspar, Ca-sulfate, Ca-phosphate, Fe-sulfide,
35 and fluorite.

36 Breccias, formed during collapse of some the miarolitic cavities, contain decaying OM, which
37 released high concentrations of dissolved NH_4^+ , responsible for the late-stage formation of
38 buddingtonite and tobelite-rich muscovite. The age of the fossils can be restricted to the time
39 between the pegmatite formation, at ~ 1.760 Ga, and the breccia formation at ~ 1.49 Ga. As
40 geological environment for growth of the microorganisms and fossilization we assume a geyser
41 system, in which the essential biological components C, N, S, and P for growth of the organisms
42 in the miarolitic cavities were derived from microorganisms at the surface. Fossilization was
43 induced by magmatic SiF_4 -rich fluids. The Volyn occurrence is a distinct and uncommon

- 44 example of Precambrian fossils and the results underline the importance of cavities in granitic
- 45 rocks as a possible habitat for microorganisms preserved in the deep biosphere.
- 46
- 47 Key words: microfossils, fossilization, Precambrian, pegmatite, deep biosphere

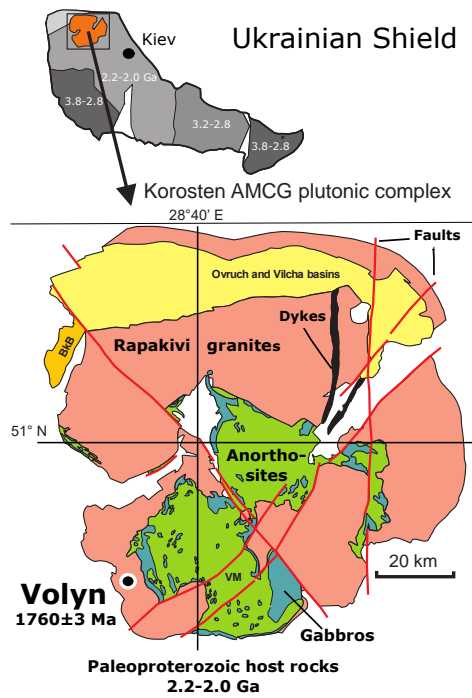
48 1. Introduction

49 Precambrian fossils are rare and their morphology is generally not well preserved. They occur
50 mostly in (meta)sedimentary rocks, but in recent years it became evident that pores, fissures
51 and other open spaces in igneous rocks can be a habitat for microorganisms (Ivarsson et al.,
52 2020). In miarolitic cavities in pegmatites from the Volyn pegmatite district, Ukraine,
53 genetically associated with the Paleoproterozoic Korosten pluton of the western Ukrainian
54 shield (Fig. 1), fossils occur in a conspicuous filamentous form. They are known as 'kerite' and
55 were first described by Ginzburg et al. (1987) as a result of abiogenic sublimation and
56 polymerization of volatile hydrocarbons from the pegmatite. In Ukrainian-Russian literature
57 this type of organic matter (OM) was characterized as (oxy)kerite, i.e. highly mature OM.
58 Gorlenko et al. (2000) and Zhmur (2003) were the first to re-interpret these kerites as fossils of
59 filamentous cyanobacteria, based on electron microscopic investigations on ultra-thin sections.
60 They also pointed out that cyanobacteria are not the only microorganisms, but they described
61 the occurrence as a microbial community, an 'Early Proterozoic autonomous biocoenosis'.
62 Stable $\delta^{13}\text{C}$ isotope ratios ≤ -40 ‰ of such filaments are similar to $\delta^{13}\text{C}$ isotope ratios in
63 methanogenic bacteria (Franz et al. 2017). Typical for kerite is the high N-content, which goes
64 up to 9 wt% (Luk'yanova et al., 1992; Franz et al., 2017). The maximum age of the fossils is
65 restricted by the 1760 ± 3 Ma intrusion age of the pegmatites (Shumlyanskyy et al., 2021; Fig.
66 1). The minimum age is constrained by ^{40}Ar - ^{39}Ar laser-ablation age data of minerals in a
67 breccia, which formed after consolidation of the pegmatites. This breccia contains degraded
68 OM together with newly formed muscovite (formation age 1491 ± 9 Ma; Franz et al., 2021) and
69 buddingtonite, NH_4 -feldspar (minimum age of 563 ± 14 Ma). Ammonium ions are a product of
70 the degradation of OM, and the white mica age and the buddingtonite age restrict the age of the
71 organisms most likely near to 1.5 Ga, the age of pseudomorph formation (for detailed
72 discussion see Franz et al., in press). (*Footnote: In the title of Zhmur, 2003, there is an obvious*

73 *typing error: It says "Origin of Cambrian fibrous kerites of the Volyn region", but in the text it*
74 *is clear that the authors refer to a Precambrian age.)*

75 The miarolitic cavities hosting the kerite fossils (Fig. 2) are a special feature of these pegmatites,
76 which are therefore referred to as 'chamber pegmatites' (see reviews in Ivanovich and
77 Alekseevich, 2007; Lyckberg et al., 2009). These chambers are zones of free growth for crystals
78 ('crystal pockets') and were formed in the cooling stage of the pegmatite, in the same way as
79 common miarolitic cavities, i.e. from magmatic fluids, liberated during crystallization. What is
80 unusual is their size: Lyckberg et al. (2019) describe the largest pocket of pegmatite no. 521 in
81 a depth of 96 m with dimensions of 45 m in length, up to 25 m wide and about 20 m high.
82 Common are cavity dimensions of 4 to 6 m in length, 3 to 4 m wide, and 1 to 3 m high (Ivanov
83 and Alekseevich, 2007), and the unusually large size is attributed to the long cooling history in
84 the order of millions of years of the Korosten pluton with supply of fluids from anorthositic
85 magmas (Shumlyanskyy et al., 2021).

86 A striking feature of kerite is the well-preserved morphology (Zhmur, 2003; Franz et al., 2017),
87 which poses the question how the delicate OM without skeletal parts in the organisms was
88 fossilized. Zhmur (2003) interpreted this process as 'hydrocarbon-aqueous fossilization' due to
89 prolonged low-temperature dehydration and oxidation. Here we present data from reflected
90 light microscopy, scanning electron microscopy (SEM), transmission electron microscopy
91 (TEM), and electron probe microanalysis (EMPA) to show that the fossilization process is
92 mainly driven by the reaction of Si-Al-(Ca) with the organisms via a fluid phase rich in F, Cl,
93 S, and P, followed by encrustation of Al-silicates. Attempts to directly date black opal with
94 inclusions of OM and of filamentous kerite using U-Pb-systematics resulted, in the case of opal,
95 in scattered U-Pb data indicative of open system behavior. For the filamentous kerite we
96 obtained a nominally Cambrian minimum age that is consistent with the inferred Precambrian
97 age.



99

100 **Figure 1: Location of the Volyn pegmatite field in the Korosten anorthosite-mangerite-**
 101 **charnockite-granite plutonic complex, north-western Ukrainian Shield (numbers refer to**
 102 **the ages in Ga of consolidation of the shield; Shumlyanskyy et al., 2017). The pegmatite**
 103 **age of 1760±3 Ma at Volyn refers to zircon U-Pb SIMS data (Shumlyanskyy et al., 2021).**

104

105 **1.1 Sample material and methods**

106 Sample material from the Volyn pegmatite includes kerite, obtained from the Museum of the
 107 National Academy of Sciences, Semenenko Institute of Geochemistry, Mineralogy and Ore
 108 Formation, Kyiv, and seven kerite samples, sampled underground in situ from the pegmatites
 109 (Table 1). Kerite could not be found in the surrounding granite, only in the pegmatite. The
 110 microfossils are found free on the surface or partly in the upper layer of clay on the floor of the
 111 miarolitic open chamber (Fig. 2). Kerite occurs there in masses of kg and as described in the
 112 Russian and Ukrainian literature (Zmuhr 2003, Gorlenko et al. 2000, and references therein),
 113 as verified by coauthor Chernousenko. It can be found also on the surface of beryl and topaz
 114 crystals.

115 In addition, we investigated single crystals of beryl with etch pits, which contain kerite, and use
116 data from a previously investigated sample 2008-V (Franz et al., 2017), a breccia collected from
117 the mine tailings of pegmatite no. 2, which contains degraded OM in a pseudomorph after beryl,
118 consisting of buddingtonite, muscovite, betrandite, and opal. For the age determination, we
119 used this OM together with sample #9 (Table 1; aliquots a,b,c), which is topaz with degraded
120 OM, and black opal (sample BO, subdivided into aliquots) from the same shaft.



121
122 **Figure 2: (a) Kerite-rich in situ occurrence (black; arrows) on wall inside crystal cavity**
123 **chamber in shaft 3 of Volyn Chamber Pegmatite, Volyn Piezo Quartz Deposit,**
124 **Korosten Pluton, Zhitomirskaya Oblast, Ukraine, with chief geologist Vsevolod**
125 **Chournousenko as scale.**
126 **(b) Black kerite in situ on wall inside crystal cavity chamber. Photos courtesy of V.**
127 **Chournousenko.**

128
129 SEM images were obtained with a Hitachi SU8030 instrument, equipped with an EDAX EDS
130 system with a 30 mm² silicon drift detector (SDD) fitted with a silicon nitride window. We first

131 tried to work without coating but the filaments are non-conductive and were electrically
 132 charged. Samples were therefore coated with an approximately 5 nm thick Ir layer allowing for
 133 high-resolution imaging of the filaments' surfaces without a structure of the commonly applied
 134 Au coating. The kerite filaments without further cleaning or preparation were mounted on Al
 135 stubs stickered with conductive carbon tabs. The beryl crystals with kerite filaments were dust-
 136 cleaned with compressed air and coated with C.

137

138 Table 1: List of samples and their macroscopic appearance

No./GFZ no.	Year of sampling	Material	Location	Morphology
0/Museum Ac. Sci. Kyiv	unknown	kerite	unknown	filamentous
1/G017809	2018	kerite	shaft 3	filamentous
2/G017810	2018	kerite	shaft 3	filamentous
3/G017811	2018	kerite	shaft 3	filamentous
4/G017812	2018	kerite	shaft 3	filamentous, spherical
5/G017813	2013	kerite	shaft 3	flaky, botryoidal
6/G017814	2013	kerite	shaft 3	filamentous, flaky
7/G017815	2013	kerite	shaft 3	filamentous, spherical
2008-V-10	2008	beryl crystal with etch pits	mine tailings pegmatite #2	filamentous, spherical, flaky
9a,b,c	2018	topaz with kerite	shaft 3	(degraded kerite)
BO	2018	black opal	shaft 3	(inclusions of OM)
2008-V- 1,a,b,c	2008	pseudomorph after beryl	mine tailings pegmatite #2	(degraded kerite)

139

140 The JEOL JXA-8530F field emission microprobe at TU Berlin was used to investigate the same
 141 mounts that were used for reflected light microscopy, but with C-coating, for quantitative
 142 results and less absorbance (compared to Ir). EPMA data for element distribution maps of cross
 143 sections or of parts of the rim of the filaments and flaky kerite in the wave-length dispersive
 144 mode of the microprobe were acquired using an 8 kV, 20 nA beam with a probe diameter of 64
 145 nm. Back-scattered electron images (BSE) were taken to select appropriate sites. Mappings
 146 were done in stage scan-modus with pixel resolution between 277 and 360 x 180 and 265, with

147 a pixel size of mostly 80 nm, and a dwell time per pixel of 200 ms. Total scan areas varied
148 between 70 x 36 μm to 33.2 x 31.8 μm .

149 Open-system pyrolysis was performed using a Quantum MSSV-2 Thermal Analyzer©
150 interfaced with an Agilent GC 6890A gas chromatograph. Milligram quantities (0.3-2.0 mg) of
151 freshly powdered sample material were weighed into the central part of small glass capillaries
152 and fixed with purified quartz wool that had been cleaned by heating at 630°C in air for 30 min.
153 Open-system pyrolysis was performed from 300°C to 600°C at 40°C/min in a flow of He at a
154 rate of 30 mL/min. The generated hydrocarbons were immediately transferred to a liquid
155 nitrogen cooled trap and subsequently analyzed using an Agilent GC 6890A gas chromatograph
156 equipped with an HP-Ultra 1 column of 50 m length, 50m x 32mm internal diameter,
157 dimethylpolysiloxane-coated column (0.52 μm film thickness), and flame ionization detector.
158 The oven temperature was programmed from 30°C to 320°C at 5°C/min. Qualification of single
159 compounds was conducted using reference chromatograms.

160 For the U-Th-Pb analysis, fragments of OM from two samples were selected under a binocular
161 microscope. Fragments from sample No. 9 were visually pure, inclusion-free, with a dark
162 brownish color. Fragments from sample No. 1 showed fine-grained intergrowth with colorless
163 to whitish phases, probably quartz and feldspar. After cleaning in double-distilled water in an
164 ultrasonic bath, fragments (weight between 0.38 and 2.53 mg) were digested in 68%-HNO₃ at
165 220°C for 48 h using a Parr-type hydrothermal digestion vessel, a procedure that has been
166 shown to effectively mineralize a broad range of organic matter (Tahán et al., 1993). Optical
167 control revealed that all OM was fully dissolved in this step. Sample solutions were dried and
168 re-dissolved in 2%-HNO₃. Concentrations of U and Th were measured by isotope dilution on a
169 Thermo Scientific ELEMENT XR ICP-MS at GFZ Potsdam, using a mixed ²³⁵U-²³⁰Th spike.
170 Concentrations of lead isotopes ²⁰⁴Pb, ²⁰⁶Pb, ²⁰⁷Pb, and ²⁰⁸Pb were determined on the same
171 instrument from sample signal count rates compared to an external calibration curve for Pb.

172 Corrections for background and for interference of ^{204}Hg on the ^{204}Pb signal were applied.

173 For TEM investigations foils were prepared using focused ion beam (FIB); for details of milling
174 see Wirth (2004, 2009). The foils were studied in a Tecnai F20 X-Twin TEM operated at 200
175 kV with a field emission gun as electron source, equipped with a Gatan imaging filter GIFTM
176 (Tridiem), a Fishione high-angle annular dark field detector (HAADF), and an EDAX X-ray
177 analyzer with ultra-thin window. Bright field, dark field and high-resolution TEM images are
178 usually acquired as energy-filtered images applying a 20 eV window to the zero loss peak of
179 the electron energy-loss spectrum. Counting time for EDS analyses (processed with TIATM
180 software) in the scanning transmission mode across a pre-selected area thus avoiding mass loss
181 during the data acquisition, was 60 to 120 s. Electron diffraction data were acquired as selected
182 area electron diffraction pattern (SAED) or derived from high-resolution lattice fringe images
183 applying a fast Fourier Transform (FFT). Electron energy loss spectra (EELS; data processing
184 with Digital MicrographTM) were acquired in diffraction mode using a camera length of 700
185 mm. Applying a 1 mm entrance aperture the resulting acceptance semi angle is 5 mrad.
186 Dispersion was 0.1 eV/pixel, acquisition time was 1 s.

187

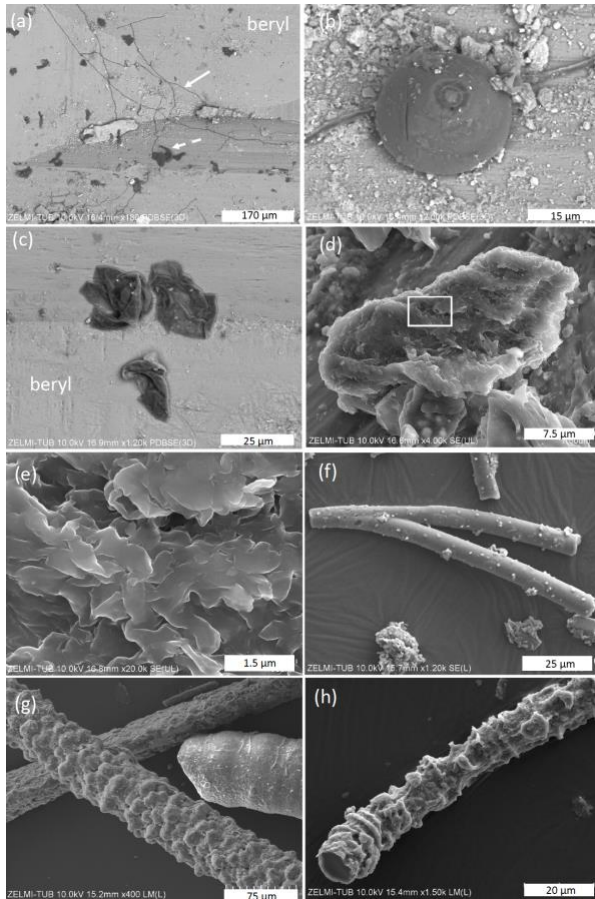
188 **2 Results**

189 **2.1 SEM images**

190 The kerite morphology is best illustrated in SEM images (Fig. 3). There are three different types
191 of morphologies, classified as filamentous, often branched (Fig. 3a,c), as spherical (Fig. 3b),
192 and irregular, flaky objects (Fig. 3c). Objects with spherical morphology are rare, therefore we
193 restrict to the filaments and flakes, which could also be found in thick sections of kerite
194 embedded in epoxy, and thus available for more detailed analytical investigations. Filaments
195 are the dominant forms. Broken pieces are up to ~1 cm long and have a variable diameter, from
196 1-2 μm up to c. 80 μm , mostly near c. 15-20 μm . Many of the filaments are branched (Fig. 3d),

197 or segmented (Fig. 3e,f) and show globular outgrowths, some of these outgrowths with
198 botryoidal shape (Fig. 3e). This botryoidal shape can extend into more irregular, ridged forms.
199 Flaky kerite is best seen in etch pits of beryl from Volyn (Fig. 3a,c), attached together with
200 filamentous and rare spherical objects to the surface of beryl.

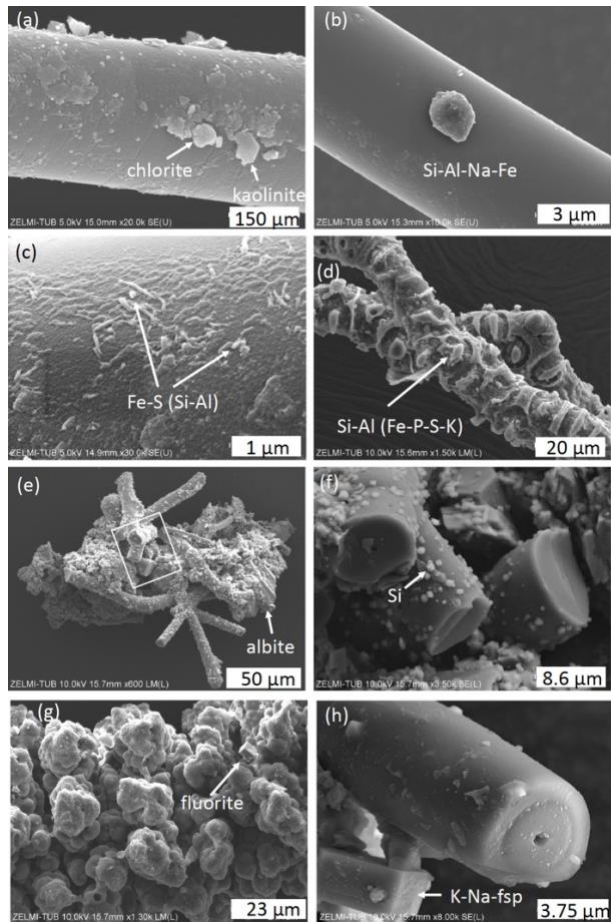
201 In many cases we see minerals grown onto the filaments, identified by chemical composition
202 and shape as e.g. kaolinite and chlorite (Fig. 4a), illite and Na-Al-silicate (Fig. 4b); for
203 documentation of the EDS spectra see Supplementary Information Fig. S1. On filaments with
204 a rather smooth surface we see structures in the order of 100 x 500 nm which are enriched in
205 Al, Si, Fe, and S, probably pyrite/markasite with Si-Al-incrustations (Fig. 4c). Segmented
206 filaments (Fig. 4d) show larger structures and the EDS analysis indicates incrustations of clay
207 minerals such as illite/kaolinite. In many spectra, the peak of Ir is relatively broad and this might
208 be an indication for overlapping with a P-peak. As we show later (results of EMPA), P is indeed
209 present in the kerite rims. The matrix between filaments consists of opal, intergrown with
210 silicates, probably Na-feldspar, and clay minerals (Fig. 4e,f). In several cases, fluorite crystals
211 could be identified together with the incrustations. In this case, there are also traces of Ca in the
212 incrustation.



213

214 **Figure 3: SEM images of kerite fossils, illustrating the different morphologies. (a)**
 215 **Filamentous and flaky kerite in etch pits of beryl (sample #10). (b) Spherical object on a**
 216 **filament (sample #10). (c) Flaky kerite (sample #10). (d, e) enlarged particle of flaky**
 217 **kerite; white rectangle indicates position of (e). (f) Branched filament with smooth surface**
 218 **(sample #4). (g) Filaments with a botryoidal and a smooth, slightly segmented surface**
 219 **(sample #5). (h) Fiber with a strongly segmented surface (sample #2). EDS-spectra of flaky**
 220 **kerite are shown in Fig. S2.**

221



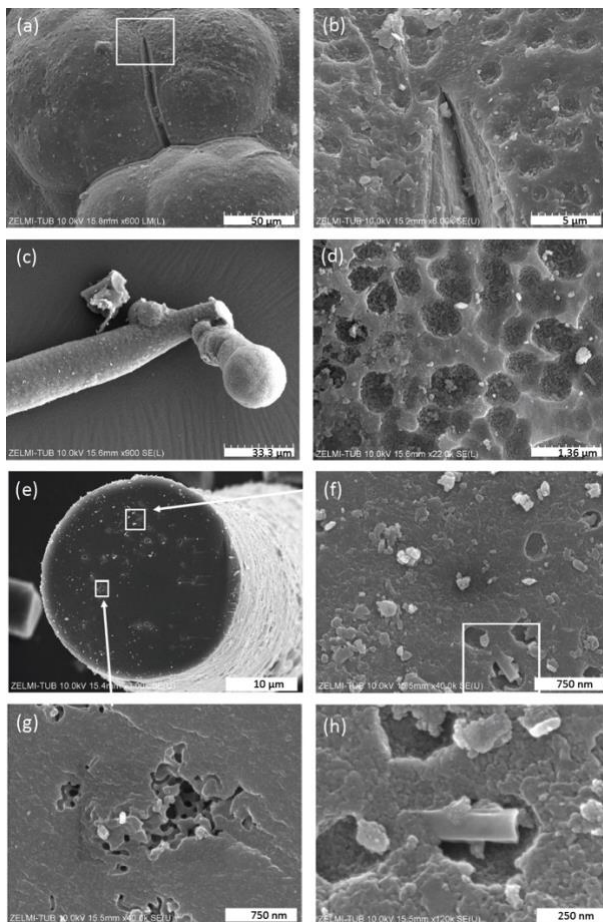
222

223 **Figure 4: SEM images of minerals, associated with kerite. (a) Chlorite and kaolinite, and**
 224 **(b) unidentified Na-Fe-Al-silicate grain grown onto a filament (sample #0). (c) High-**
 225 **magnification of filament surface with Fe-sulfide (pyrite/markasite?) and incrustations of**
 226 **Si-Al (sample #0). (d) Incrustation on segmented filament, with dominantly Si-Al, minor**
 227 **peaks of Fe-P-S-K (sample #4). (e) Aggregate of filaments, cemented by minerals; lower**
 228 **right is an albite crystal; rectangle shows position of (f), enlarged part with broken**
 229 **filaments and small opal grains (identified by a Si-peak and globular shape) attached to**
 230 **the surface (sample #4). (g) Aggregates forming a botryoidal surface of a filament,**
 231 **intergrown with a fluorite crystal. (h) Alkalifeldspar, grown onto a broken filament with**
 232 **central cavity.**

233

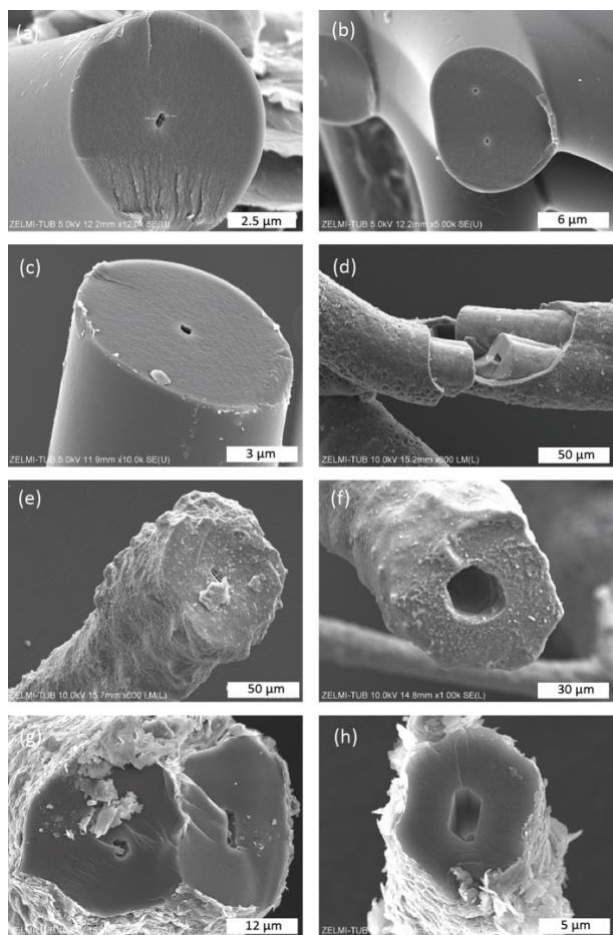
234 The surface of botryoidal shapes (Fig. 5a) shows μm -wide gaps, explained as shrinking cracks,
 235 and ball-shaped outgrowths (Fig. 5b,c) with a dented surface, interpreted as a result of degassing
 236 of the OM. The EDS-spectra of this surface shows peaks for Al and Si, in addition to the C-N-
 237 O-content of kerite. The internal structure of kerite is seen in a broken face of a filament; it is
 238 characterized by a porosity (Fig. 5e-h), also interpreted as result of degassing. Individual pores
 239 are irregular in shape and in the order of several 100 nm large (Fig. 5g,h). In cross section, some
 240 of the broken filaments show a central cavity, i.e. a channel extending along the filament axis

241 (Figs. 4h, 6). The cross sections of this channel vary from c. 250 x 500 nm (Fig. 6a) to c. 20 x
 242 20 μm (Fig. 6f) in diameter. In some cases, the channel has a six-sided outline (Fig. 6f,g,h).
 243 The fractured surface with fringe fractures, sub-perpendicular to the filament length (Fig. 6a,g),
 244 indicates brittle behavior of the filaments, which was also observed during handling the
 245 individual filaments for preparation. Figure 6d shows a broken filament with a sheath-like outer
 246 part. The outer rim (with a dented surface, seen in its lower part) contains some Al-Si, a small
 247 amount of K and possibly P (Fig. S4 analyses 2 & 5); the inner rim shows only traces of Al-Si,
 248 but some U (analyses 3 & 4), whereas the center near to the channel (analysis 6) shows only
 249 the peaks of C-N-O, characteristic for kerite. The count ratios for C/O increase systematically
 250 from outer rim to the center (Fig. S4).



251

252 **Figure 5: SEM images of surfaces of kerite. (a) Botryoidal surface with a shrinking crack;**
 253 **inset shows enlarged part in (b) with a dented surface (sample #5). (c) Ball-shaped end of**
 254 **a filament, with (d) dented surface (sample# 1). (e) Broken filament (sample #3), showing**
 255 **internal porosity (f,g,h) with irregular outlines, of a few hundreds of nm wide. White**
 256 **rectangle in (f) indicates enlarged part shown in (h).**



257

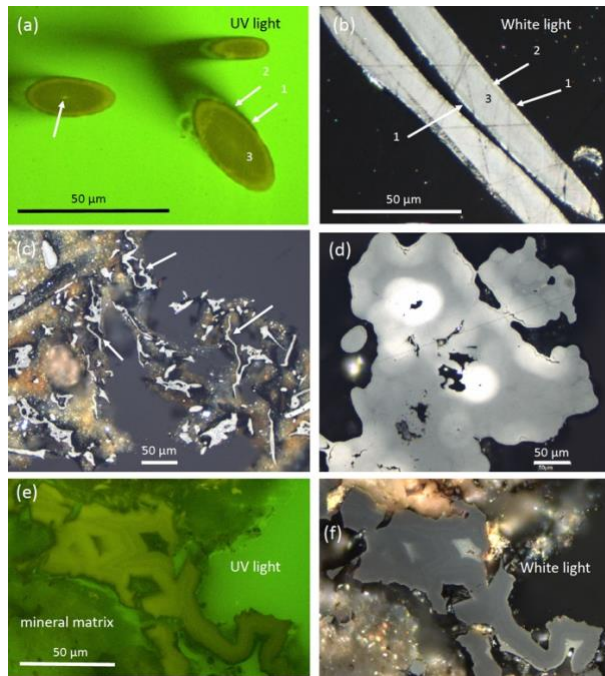
258 **Figure 6: SEM images of broken filaments, showing a central channel. (a) Six-sided**
 259 **channel with dimensions 260 x 550 nm of filament with a smooth surface, and fringe**
 260 **fractures on the broken face, indicating brittle behavior. (b) Double channel, probably**
 261 **initial crosscutting of a branching (cf. Fig. 4d). (c) Similar channel as in (a), but less**
 262 **regular outline (all sample #0). (d) Filament with a central part, a sheath-like outer part,**
 263 **and a channel; numbers refer to analysis points (see text; EDS spectra in Fig. S4). Note**
 264 **dented surface in lower part of the sheath-like outer part (sample #5). (e) Filament with a**
 265 **rough surface and a channel 4 x 11 μm. (f) Large, ca. 25 μm wide channel with six-sided**
 266 **outline (both sample #5). (g,h) Filaments with encrustations of clay minerals and six-sided**
 267 **channels (sample #7).**

268

269 **2.2 Reflected light microscopy**

270 In two-dimensional cuts in polished mounts in epoxy, observed under UV light for fluorescence
 271 and under white light for reflectivity (Fig. 7), the clear outer circular (to elliptical in oblique
 272 sections) shape of filaments is obvious in cross sections (Fig. 7a). In longitudinal sections (Fig.
 273 7b), the symmetrical internal structure, which shows up in the cross sections, extends along the
 274 whole filament. There are mainly three zones, an outer discontinuous, thin rim with a higher

275 reflection/lower luminescence (zone 1), followed by a zone 2 with poorer reflection, higher
 276 fluorescence, and a core zone 3 with low fluorescence/intermediate reflectivity. The central,
 277 open channel with different width is also seen in many filaments (Fig. 7a). Ball-shaped
 278 outgrowths show the same type of zoning as the filaments. Flaky kerite is seen as a thin (a few
 279 μm wide) (bio?)film, intergrown with mineral matrix (Fig. 7c). Botryoidal shapes show
 280 difference in reflectivity which runs parallel to the surface (Fig. 7d) and with highest reflectivity
 281 around pores. Thick, irregularly shaped masses, possibly degraded OM (Fig. 7e,f) show rims
 282 high in reflectance and zonal distribution of luminescence in UV light.



283

284 **Figure 7: Optical reflected light microscopy of polished grain mounts, under UV light for**
 285 **fluorescence and under white light for reflectance. (a) Cross section of filaments, with a**
 286 **central channel (left arrow) and three zones of fluorescence. (b) Longitudinal sections**
 287 **show a symmetrical distribution of the three zones in reflectance, where the rim with high**
 288 **reflectance corresponds to the rim with low fluorescence shown in (a). (c) Thin flaky**
 289 **kerite, interpreted as former biofilms (arrows). (d) Botryoidal kerite with zonal**
 290 **distribution of reflectivity. (e, f) Thick masses of flaky kerite with zonal fluorescence and**
 291 **reflectivity.**

292

293 2.3 Electron microprobe analyses (EMPA)

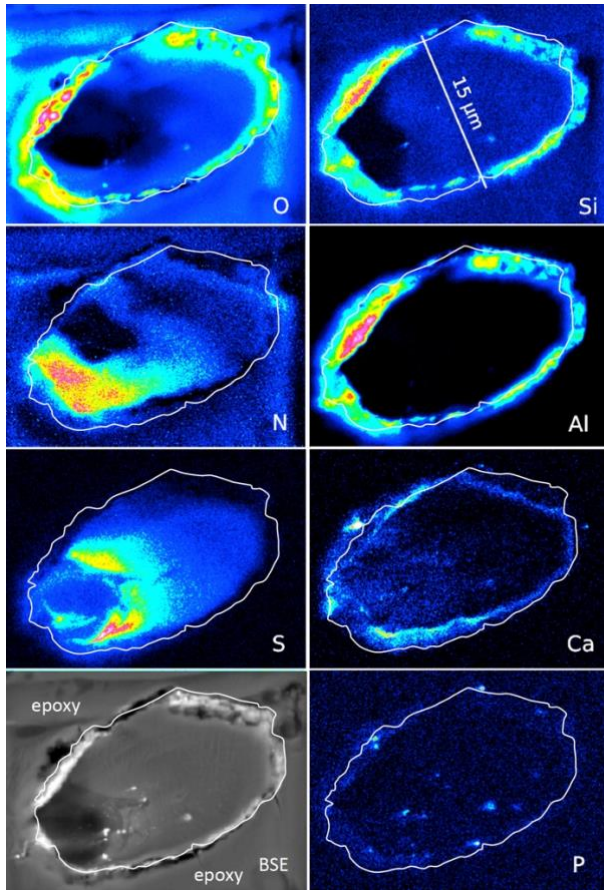
294 The same mounts prepared for reflected light microscopy were used for EMPA. Within the
 295 mineral matrix, we confirmed the presence of fluorite, closely intergrown with kerite, and also

296 identified buddingtonite, characterized by zoning and a significant decrease of the NH₄-
297 component from core to rim (Fig. S4).

298 In order to show the distribution of elements in kerite by element mapping with EMPA, we
299 chose two cross sections of filaments (Fig. 8); the outer part of a large, segmented filament (Fig.
300 9); a botryoidal part with ball-shaped outgrowths on more irregularly shaped kerite; and the rim
301 of flaky kerite (Fig. 9). BSE images for location of the mapping areas in the selected grains are
302 shown in the Fig. S5. Mapping included the characteristic elements identified before with SEM-
303 EDS, i.e. O-N as part of kerite (C was not mapped because samples were C-coated), S and P,
304 which can be part of kerite, but were also observed on the surface as sulfate or phosphate
305 minerals (see above, SEM investigations), and Si, Al, and Ca as characteristic for silicates. Cl
306 was mapped, because we found it also on the surface of the OM in the etch pits in EDS analysis,
307 but was below detection level in the element distribution maps. Because the OM is very
308 sensitive to the electron beam (see image after mapping in Fig. S5c), we chose a trade-off
309 between high resolution, X-ray excitation, and measuring time, but nevertheless, beam-related
310 damage could not be completely avoided.

311 An oblique section of a 15 µm-wide filament (Fig. 8) shows O enriched in the upper right part,
312 where N and S are low, indicating simultaneous N and S loss during progressive maturation.
313 During maturation of OM labile nitrogen and sulfur-bearing compounds are converted and lost
314 whereas oxygen-bearing macromolecules are enriched (Poetz et al., 2014). Here, mineralization
315 of the organic fraction was preservative due to aromatization and this process caused formation
316 of oxygen-bearing aromatic macromolecules. However, S is low in the area in the lower left
317 with lowest BSE-contrast and where N is concentrated. Si and Al concentrated in the outer,
318 irregular and discontinuous rim, together with O, present as Al-silicates as determined by SEM.
319 The Ca-distribution is complex; it is enriched in the rim, but does not follow Si-Al. Instead, it
320 forms an inner rim. It is also concentrated in the lower left part of this filament, in the same

321 area, where S is enriched. P shows some enrichments in spots in the inner part and in the rim,
322 together with Ca interpreted as Ca-phosphate. Similar element distributions were observed in a
323 circular section of a filament (Fig. S6).



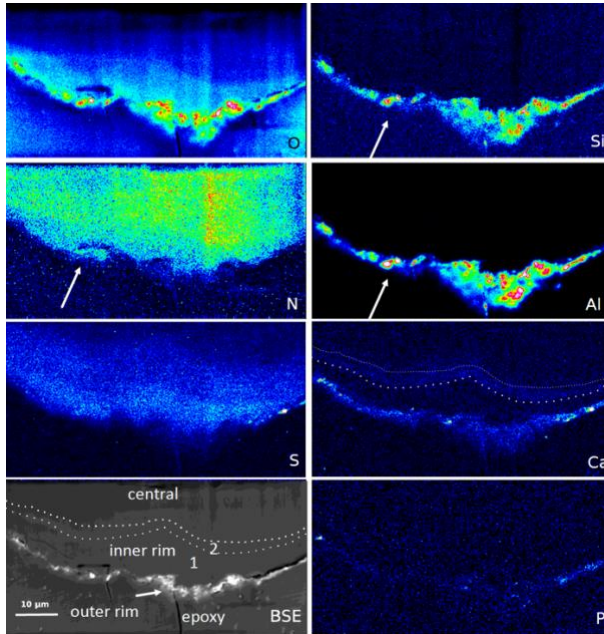
324

325 **Figure 8: Element distribution (EMPA) of an oblique section of a 15 μm-wide filament,**
326 **embedded in epoxy. White line indicates outermost rim of the filament, as seen in the BSE**
327 **image. BSE-contrast is lowest in the area of low O, high N content. Si and Al (with O)**
328 **form an outer rim, indicating Al-silicates (probably clay minerals, as determined by**
329 **SEM). Ca is also concentrated in the rim, but also in spots together with P and in the area**
330 **with high S. Scanning conditions: pixel resolution of 360 x 265, pixel size of 80 nm, dwell**
331 **time per pixel of 200 ms, total scan area 28.8 x 21.2 μm.**

332

333 The outer rim of a segmented filament (Fig. 9) allows a sharper differentiation compared to the
334 observations above: Si, Al, O are concentrated in the outer, irregular and discontinuous rim,
335 together with Ca, which is enriched in spots together with P, but also with S (probably forming
336 Ca-sulfate); S is enriched together with Ca in the outer rim. The outer rim is followed by an
337 inner rim 1, poor in Ca, and then by an inner rim 2 with Ca-enrichment. O distribution is highest

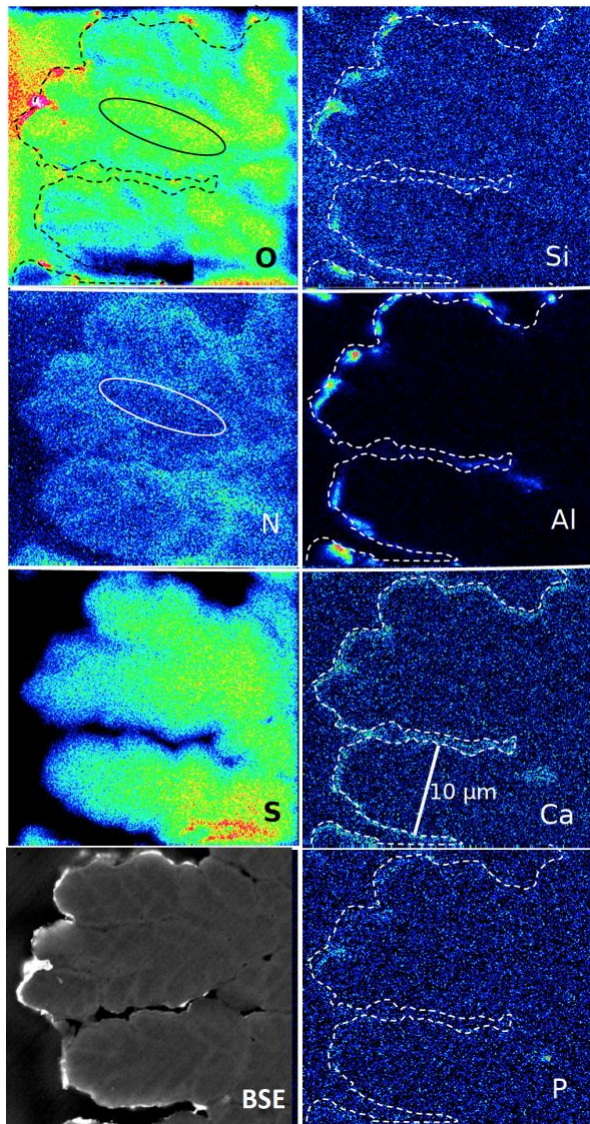
338 in the outer rim, high in the inner rim 1 with a rather sharp boundary to the inner rim 2, and
 339 then diffuse into the central part. N shows a relatively homogeneous distribution, but occurs up
 340 to the outer rim in areas of Si-Al concentrations, indicating the formation of NH₄-minerals
 341 (buddingtonite, tobelite).



342

343 **Figure 9: Element distribution (EMPA) of the rim of a large filament. The rim consists of**
 344 **three areas, best visible in the BSE and Ca image: an outer, irregular and discontinuous**
 345 **rim with enrichment of Si-Al-O and Ca, an inner rim 1, poor in Ca, followed by an**
 346 **approximately 1-2 μm wide inner rim 2, enriched in Ca (dotted lines). In the outer rim,**
 347 **Ca is also concentrated together with P and S. N distribution is relatively homogeneous,**
 348 **but notably extends up to the outer rim, together with Al-Si (arrows), indicating**
 349 **formation of NH₄-minerals (buddingtonite, tobelite). Vertical stripes are due to beam**
 350 **damage. Scanning conditions: pixel resolution 350 x 180 with pixel size of 200 nm and a**
 351 **dwell time per pixel of 200 ms, total scan area 70 x 36 μm.**

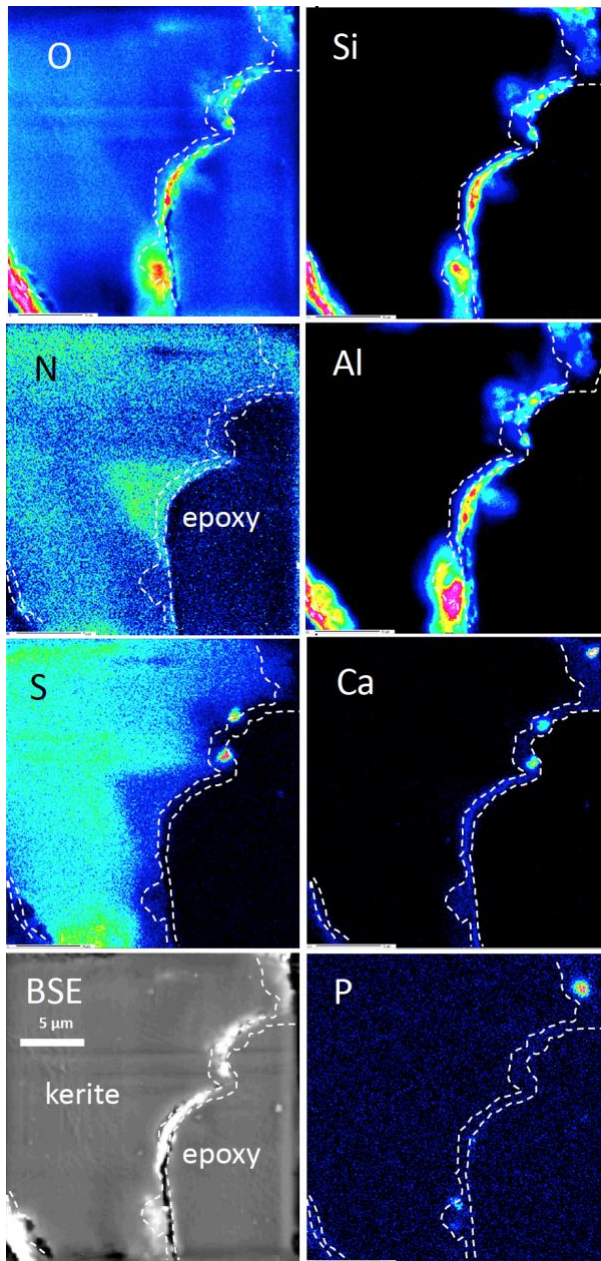
352



353

354 **Figure 10: Element distribution (EMPA) in botryoidal kerite. The rim (dashed line) is**
 355 **outlined as seen in the BSE image. Si, Al, and O are concentrated in a discontinuous rim,**
 356 **indicating Al-silicates. Ca is concentrated in spots in this rim together with P, indicating**
 357 **Ca-phosphate. Sulfur decreases systematically from the central part to the rim. N**
 358 **distribution is heterogeneous, and mimics the BSE contrast. Areas rich in O are poor in**
 359 **N (see oval outlined area). Scanning conditions: pixel resolution of 277 x 265 with pixel**
 360 **size of 120 nm and a dwell time per pixel of 200 ms, total scan area 33.2 x 31.8 µm.**

361



362

363 **Figure 11: Element distribution (EMPA) of the rim of flaky kerite. The rim is outlined as**
 364 **seen in the Ca image. Si, Al, and O are concentrated in a discontinuous rim, indicating**
 365 **Al-silicates. Ca is concentrated in spots together with P and S, indicating Ca-sulfates and**
 366 **Ca-phosphates, but also in a continuous rim with concentrations slightly above the**
 367 **background. Sulfur - except for the enrichment in spots - is absent in this area, and also**
 368 **less concentrated near to the rim. N distribution is heterogeneous, but as in Fig. 9 can**
 369 **extend up to the outer rim. Areas rich in N are poor in O.**

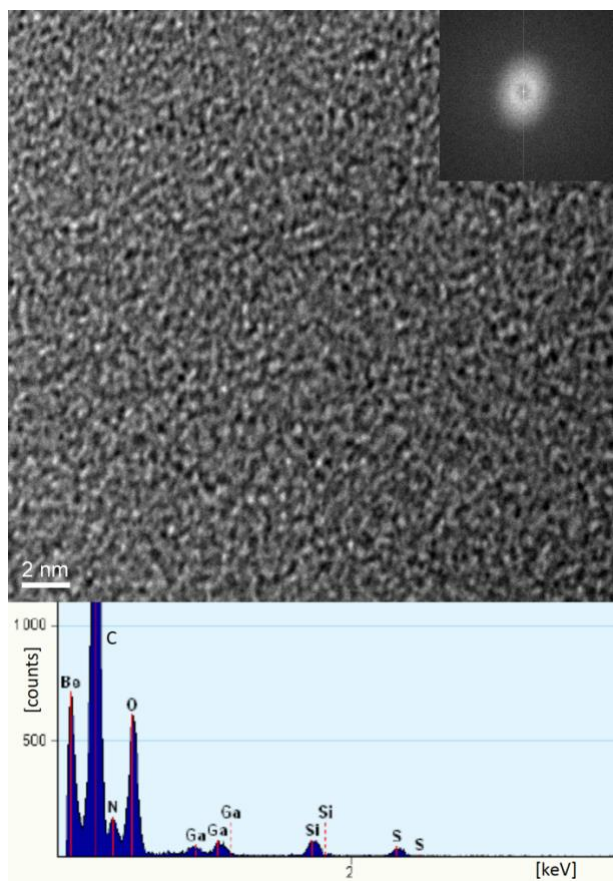
370

371 The element distribution in botryoidal kerite (Fig. 10) is characterized by an internal,
 372 heterogeneous N distribution, anticorrelated with O, which is visible in the BSE contrast. Sulfur
 373 systematically decreases from the central part towards the rim. Calcium is enriched in a thin
 374 rim, associated with P in a few spots as Ca-phosphate. The element distribution in flaky kerite

375 (Fig. 11) is generally similar to the observations made in filaments. Al-silicates form an outer,
376 discontinuous rim, Ca is slightly above the background in the rim, but also forms discrete, small
377 ($\leq 1 \mu\text{m}$) Ca-sulfates and Ca-phosphates. Sulfur is absent (except for the enrichment in Ca-
378 sulfates) in this rim, indicating loss of S during maturation/fossilization. Towards the interior
379 of the flaky OM, distribution of N, O, and S is heterogeneous, a possible indication for a primary
380 (biological) character, combined with loss of N during degradation. A different flaky object
381 shows similar element distributions (Fig. S8), however the phosphatization in the outermost
382 rim is more pronounced than in the other element distribution maps.

383 **2.4 TEM investigations**

384 TEM investigations of FIB-cut foils from a filament, with the foil cut parallel to the elongation
385 of the filament. In the center (Fig. 12) it shows the amorphous character and the presence of Si
386 together with C-N-O-S. In the rim, infiltration of Si, Al, and Ca, but in addition also Mg, Fe,
387 K, and Ni in the whole filament could be confirmed (Fig. S8); N was also confirmed by EELS
388 analysis (Fig. S8) in the dominantly C-rich matrix.



389

390 **Figure 11: HRTEM-image of central part of a filament, showing amorphous kerite (inset**
 391 **is electron diffraction pattern) and EDS-spectrum of a spot, confirming Si as an impurity,**
 392 **C-N-O and S as the kerite constituents. Ga-peak is from cutting of the FIB foil, Be is from**
 393 **the Be-sample holder.**

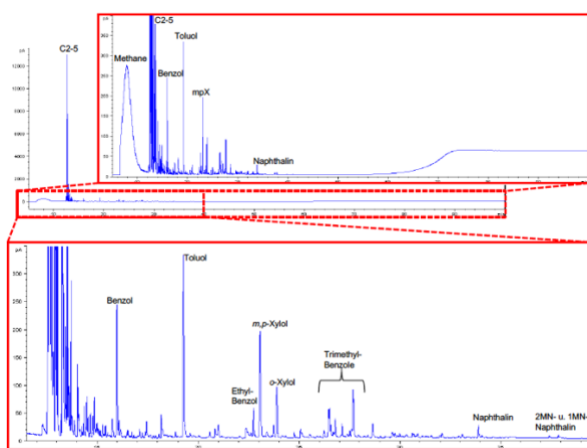
394

395 2.5 Pyrolysis

396 Results of open-system pyrolysis are consistent with other observations, indicating mature or
 397 very mature OM, and there is no essential difference between samples with well-preserved
 398 shape and others with many incrustations. The gas chromatographic fingerprints of sample #0
 399 are shown in Fig. 13, the results of the other samples are in Fig. S9.

400 All are strongly dominated by hydrocarbon gases C₁₋₅ (methane through pentane) and
 401 subordinately by alkylated mono- and diaromatic compounds. These are typical pyrolysis
 402 breakdown products of organic matter in general, but as higher n-alkyl homologues (n-C₆₊) or
 403 oxygen-, sulphur-, and nitrogen-functionalized compounds (e.g., phenols, thiophenes, and
 404 carbazoles) as indicators of biological precursor structures (Larter, 1984; Horsfield, 1989;

405 Sinnighe Damsté et al., 1989) are essentially absent they are indicative of mature OM. Loss
 406 of functional groups during diagenesis and loss of H-rich components during catagenesis leads
 407 all organic matter types to move towards the point (metagenesis) where they become
 408 indistinguishable finally possessing only a potential for the generation of dry gas (methane) and
 409 mono aromatic compounds (Tissot and Welte, 1984; Quigley and Mackenzie, 1988; England
 410 and Mackenzie, 1989; Horsfield, 1989). In line with remaining fluorescence the composition
 411 of the pyrolysate, especially presence of wet gases (C₂₋₅) and diaromatic compounds, indicates
 412 that the OM has not yet arrived at metagenesis (R_o>2.0%, where R_o = vitrinite reflectance in
 413 oil (Tissot and Welte, 1978). GC-fingerprints resemble e.g. those of Paleozoic coals and shales
 414 from Australia at 1.7% < R_o < 2.3% (Mahlstedt et al., 2014, 2015). Assuming typical geological
 415 heating rates between 1 and 3K/Myr and based on the easyR_o model (Burnham and Sweeney,
 416 1989). OM at these maturity levels must have been heated to somewhere between 175 and
 417 200°C; a similar temperature range was also derived from mineral equilibria (Franz et al.,
 418 2017). In case that peak temperatures were very short-lived, temperatures could have been
 419 slightly higher, but the time duration for the maturation of the Precambrian fossils is essentially
 420 unknown.



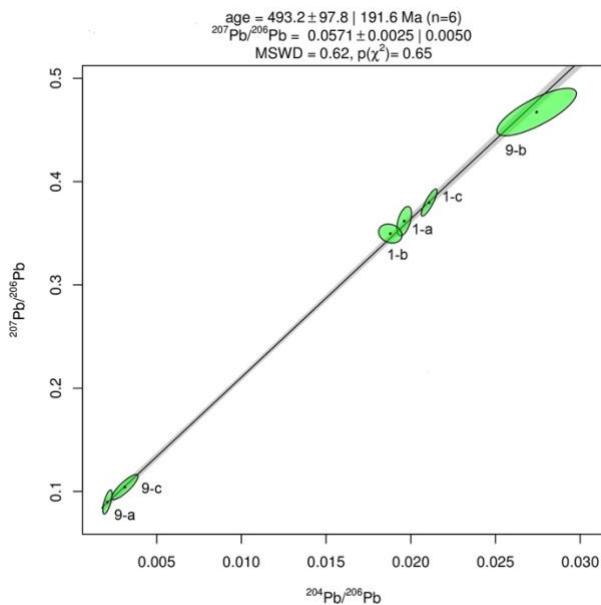
421
 422 **Figure 12: Open-system pyrolysis GC-trace of kerite (sample #0/Museum Ac. Sci. Kiev),**
 423 **is dominated by hydrocarbon gases methane through pentane and subordinately by**
 424 **alkylated mono- and diaromatic compounds, typical breakdown products of mature or**
 425 **very mature OM.**

427 **2.6 U-Th-Pb analyses**

428 Table 2: Results of Pb isotope data of aliquots of OM, sample 9 (visually pure oxykerite) and
 429 sample 1 (impure with whitish minerals)

sample	weight (g)	$^{206}\text{Pb}/^{204}\text{Pb}$	RSD%	$^{206}\text{Pb}/^{207}\text{Pb}$	RSD %	$^{208}\text{Pb}/^{204}\text{Pb}$	RSD%
UKR 1 9-a	0.00253	477.3	5.3	42.83	10.63	5.32	108.5
UKR 2 9-b	0.00090	36.46	3.5	17.04	2.132	2.01	42.46
UKR 3 9-c	0.00101	320.2	10.2	33.39	8.925	4.78	85.19
UKR 4 1-a	0.00038	51.00	0.9	18.45	2.753	1.61	70.18
UKR 5 1-b	0.00043	53.22	1.5	18.61	2.870	1.07	73.17
UKR 6 1-c	0.00067	47.43	0.9	18.01	2.634	1.41	64.14

430



431

432 **Figure 14: Results of Pb-Pb age determination of kerite from Volyn pegmatite. The**
 433 **reference line corresponds to an age of $493.2 \pm 97.8 \text{ Ma}$ (1σ). The large uncertainty is**
 434 **mainly due to very small amounts of Pb in the samples, resulting in poor ion counting**
 435 **statistics in mass spectrometry. Data plotted and age calculated using the program**
 436 **Isoplot-R (Vermeesch, 2018).**

437

438 Results of Pb isotope analyses of kerite samples 9 and 1 and the OM from the pseudomorph
 439 sample are listed in Table 2 and shown in Fig. 14. The reference line corresponds to an age of
 440 493.2 Ma , however with a large uncertainty of $\pm 97.8 \text{ Ma}$ (1σ). The apparent age is considered
 441 as a minimum age, because OM is very susceptible for U, which is likely present in the fluids
 442 circulating in the pegmatitic environment since formation of the miarolitic chambers until

443 modern times, a process that is capable to continuously reset U-Pb dates.

444 Chemical and U, Th, and Pb isotope data of black opal are presented in Tables S1 to S3. Major
445 element analyses (Table S1) in opal indicate approximately 2.5 wt% undetermined elements,
446 likely H₂O and hydrocarbons. Minor elements are Al (up to 1 wt% Al₂O₃), Na, Ca, and Fe,
447 which are present in 0.1 to 0.3 wt% oxide, whereas Ti, K, Mg, Fe, Cr, V, and Mn occur in
448 smaller amounts. The heterogeneous distribution of elements is also seen in the trace element
449 content among the three aliquots; Ba, Be, Li, Rb, Sc, Sr, Th, U, V, Zn, and Zr stand out with
450 content each above 1 µg/g in some of the aliquots. The U-Th-Pb isotope data (Table S3) indicate
451 open system behavior also for the black opal. The data show a large scatter; only two sample
452 pairs allowed calculating old ²⁰⁸Pb/²³²Th ages of 1500±46 Ma and 1279±35 Ma, respectively.

453 **3 Discussion**

454 **3.1 Fossilization process**

455 A further determination of the exact nature of the excellently preserved microbial fossils
456 requires a distinction between primary, i.e. biological, features and secondary, i.e. those
457 produced by fossilization. The nature of the fossils (bacteria, archaea, or fungi), which
458 colonized the igneous rocks, is not yet clarified; it requires more research, also with more details
459 on spherical kerite, which is in progress.

460 Kerite is highly mature, as shown by pyrolysis experiments (Fig. 13), but not transformed into
461 graphite, as shown by TEM investigations. It is completely amorphous (see in HRTEM image;
462 Fig. 12), indicating rather low temperatures during fossilization and afterwards. This is also
463 consistent with the observation that thin filaments are not completely opaque, but dark-brown
464 transparent, confirming Luk'yanova et al.'s (1992) observations. Their X-ray data of kerite
465 showed a diffuse maximum at c. 8 °θ, interpreted as a mixture of different carbohydrates with
466 O, N, and S, some graphite-like sheets, hexamethylene and polymerized carbohydrates with O.

467 The fringe fractures (Fig. 6a) show that the filament behaved brittle, i.e. the whole filament has
468 reached a similarly high degree of aromatization, which relates to high thermal maturity.

469 Alteration by progressive maturation (e.g., the oxygen pattern along interfaces or affecting the
470 whole kerite matrix) as a major feature is also seen in the element distribution (Figs. 8-11).
471 Sulfur can form Ca-sulfates, as seen in μm -sized spots in the rim, but is generally decreased
472 towards the rim; more detailed mapping of the element distribution in the outer rim area shows
473 Ca enrichment in spots parallel with S, but also with P (Fig. 9, Fig. S7), and we speculate about
474 the presence of both, Ca-sulfate and Ca-phosphate nano-scale inclusions due to infiltration of
475 Ca and reaction with of S and P. Sulfur and P were transported out of the filament and reaction
476 with Ca produced the Ca-free inner rim 1. Transport of Ca went further into the filament
477 producing the inner rim 2. Phosphatization, a common fossilization process (e.g. Briggs, 2003)
478 is thus only a minor feature. Alternatively, the Ca distribution in the outer part of the filament
479 might mimic a primary feature, preserved from their growth.

480 The distribution of Si-Al (together with O) is most conspicuous and restricted to a rim of $\sim 1 -$
481 $2 \mu\text{m}$ width (Figs. 8-11). The presence of Si-Al is confirmed by analytical data with SEM (Fig.
482 6d) and TEM (Fig. 12), and suggests that silicification is the first-order process of fossilization.
483 The patchy distribution indicates the formation of Al-silicate minerals, probably kaolinite or
484 related phases. These patches were observed on the surface of the filaments as vermicular
485 structures (Fig. 4c), some with clear development of crystal faces (Fig. 4a) and continue into
486 more coarse-grained features, which we call encrustations (Fig. 4d). Finally, the patches change
487 into intergrowths of minerals, which could be characterized by shape and chemistry as alkali-
488 feldspar, clay minerals, opal, Fe-sulfides, and fluorite (Fig. 4e-h).

489 We interpret the porosity observed on the surface of botryoidal structures and ball-shaped
490 outgrowths on filaments (Fig. 5c,d) and on a broken cross section (Fig. 5e-h) as degassing
491 features. The irregular internal pores on the scale of a few hundred nanometers indicate irregular

492 pathways of the gas, transitional towards the outer part into more regular, circular and larger
493 pores of 1 to 2 μm in diameter. We interpret cracks in the surface (Fig. 5a,b) as a shrinking
494 phenomenon, and the irregular shape of flaky kerite on the etch pits of beryl (Fig. 3a,c) as a
495 shrinking phenomenon of a formerly coherent biofilm. The outgrowths and ball-shaped ends of
496 filaments were interpreted by Zhmur (2003) as spherical swellings of the filament sheaths
497 produced by degassing. However, their size and transition to botryoidal and dented structures
498 (Fig. 5) is more consistent with an interpretation as a primary feature, because we don't see an
499 easy way to produce these features by fossilization. In addition, the cross sections (Fig. 7) of
500 these structures with regular outline of e.g. the distribution of fluorescence and the mappings
501 (Fig. 10) also indicate a primary feature. In contrast, the more irregular, ridge-like features (Fig.
502 3d), covered with platy clay minerals such as kaolinite (Figs. 3, 6g,h), seem to represent
503 strongly modified, original segmentation of the filaments during the fossilization process.

504 Many, but not all of the broken filaments show a central channel (Fig. 6), visible also in BSE
505 images of embedded filaments in cross sections, and it is the question if this is a primary or a
506 secondary fossilization feature. In small nanometer-scale channels, the ratio of the solid outer
507 part to channel is $\approx 10:1$ (in cross section, see Fig. 6a,c), and together with the observation that
508 not all filaments have this channel, it might be interpreted as a shrinking phenomenon.
509 However, in μm -sized channels the ratio goes down to $\approx 1:1$ (Fig. 6f,h), and such a high loss of
510 material during degassing seems unlikely. Furthermore, the six-sided outline, seen in small and
511 large channels, cannot be explained by shrinking. There is no reason why a cylindrical body
512 during shrinking should open a central channel with a regular outline.

513 In order to describe the infiltration process for the fossilization and the responsible fluid phase,
514 it is important to note that kerite occurs not only with the well-preserved morphology described
515 above, but also in patches of highly degraded OM, as shown in the previous description of a
516 breccia from these pegmatites (Franz et al., 2017). This OM is not only highly oxygenated (with

517 up to 40 atom% of O), but is also enriched in F (≤ 1.7 atom%), Zr (≤ 7 atom%), Sc (≤ 0.8
518 atom%), Y (≤ 2.7 atom%), and REE (sum ≤ 0.35 atom%), elements that were most probably
519 derived from the pegmatitic environment.

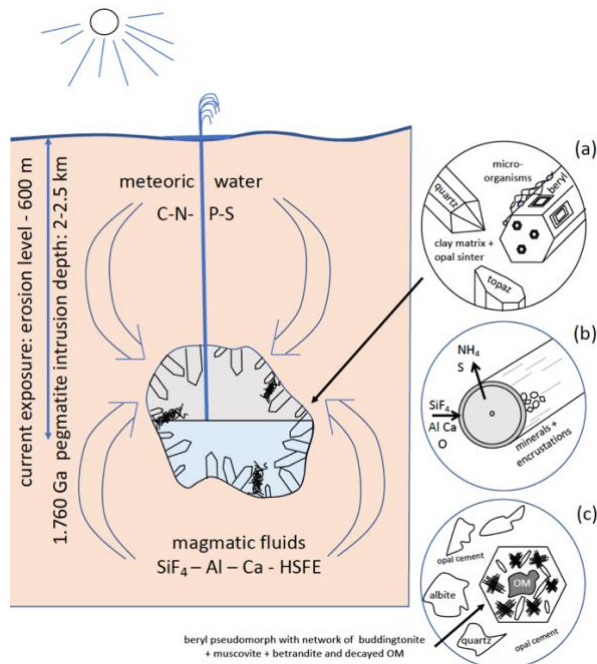
520 What is striking in all observations is the close connection between kerite and fluorite, which
521 was also described by Zhmur (2003). The whole occurrence in the granitic pegmatites with a
522 large amount of topaz in the chambers (Lyckberg et al., 2019, report that a single pegmatite,
523 no. 464, had produced 6 tons topaz in mining) points to a high concentration of F in the late-
524 magmatic to hydrothermal fluids. In addition, we observed F-rich muscovite during the
525 formation of the breccia (Franz et al., 2017) and this also points to the importance of F-activity.
526 This fluid likely carried a high amount of silica as SiF_4 (plus other components, such as Al,
527 alkalies, Ca, Mg, and Fe).

528 For the fossilization process we assume that this fluid was able to react with kerite in a depth
529 of 1-2 μm (Figs. 7-10). Gorlenko et al. (2000) and Zhmur (2003) described the outer part of the
530 filaments as a former sheath of the microorganisms. We interpret this rim area as a former thin
531 coating of biofilm that was probably very sensitive in a first stage of Si-Al-infiltration, with Ca-
532 infiltration slightly deeper into kerite. The small mineralized structures on the surface of
533 filaments (Fig. 3c) resemble what Gorlenko et al. (2000) interpreted as membrane leaflets.

534 **3.2 Environment of fossilization**

535 The geological situation for the fossilization is summarized in Figure 15. We assume that
536 fossilization must have occurred during a hydrothermal event within a fluid that carried enough
537 Si, Al, F, and Ca to react with the kerite degradation products in nano-environments. The
538 Korosten pluton intruded into continental crust, and the geological situation indicates a long-
539 living plutonic-volcanic activity (Shumlyanskyy et al., 2021), likely with near-surface geyser
540 systems. The crystallization of the pegmatites and formation of the chambers occurred in a
541 depth of 2 to 2.5 km (Lukashev, 1976, Kalyuzhnyi et al., 1971; Voznyak et al., 2007). The

542 miarolitic cavities of the granite, possibly with periodical influx of hydrothermal waters,
 543 provided the space for a continental deep biosphere, consisting probably of anaerobic,
 544 thermophilic, and acidophilic microbial species. Methanogenic microbes (indicated by C and
 545 N stable isotopes; Franz et al., 2017) might have been an important part of such a cryptic
 546 endolithic micro-ecosystem in a continental, terrestrial environment.



547

548 **Figure 15: Schematic illustration of the geological environment of pegmatites of the**
 549 **Korosten pluton, Ukraine, with m-sized miarolitic chambers and a near-surface geyser**
 550 **system. The chambers provided the space for an endolithic micro-ecosystem, which**
 551 **consists (a) of organisms with three morphologically different types (filamentous, flaky,**
 552 **and rare spherical), attached to the pegmatitic minerals, also in etch pits of beryl. (b)**
 553 **Fossilization occurs due to influx of hydrothermal fluids, carrying SiF₄ and starts with a**
 554 **µm-thin layer of Al-Si enrichment, which develops into clay minerals, feldspar, and finally**
 555 **into encrustations. (c) Strongly degraded OM is found also in breccias, formed during**
 556 **collapse of some chambers, providing NH₄ for the formation of buddingtonite, together**
 557 **with muscovite and bertrandite, in pseudomorphs after beryl.**

558

559 The flaky kerite, also visible as thin films in cross section, point to the participation of biofilms
 560 in this ecosystem, which might have developed as soon as the temperatures in the miarolitic
 561 chambers were sufficiently low for organisms to live in this environment. The essential
 562 components for the organisms - C, N, S, P - or the microorganisms themselves were transported

563 with meteoric water from the surface to the chambers. Alternatively, the components for the
564 organisms might have been transported from the metamorphic country rocks of the Korosten
565 pluton into the chambers via hydrothermal convection cells (e.g. Bobos and Williams, 2017,
566 who described NH_4 -transport for tobelite formation in a sedimentary basin).

567 Some of the miarolitic cavities collapsed and produced a breccia, which also contains degraded
568 OM and black opal with inclusion of carbohydrates (Franz et al., 2017). Chambers, which did
569 not collapse, must have been sealed. They contained a large amount of gas under high pressure,
570 and the sealing preserved the gas from escape. Lyckberg et al. (2019) reported that old log
571 books of the mining activities in Volyn describe an event in 1955, when at a depth of 600 m
572 drilling penetrated a gas-filled cavity, and as a consequence the entire drill steel shot out of the
573 hole and toppled the drill tower. It took more than 30 min, before the highly pressurized gas
574 slowed down. That a large amount of gas must have been produced during decay of the OM is
575 also indicated by the fluid-solid equilibria between NH_4^+ and K^+ , responsible for the
576 buddingtonite formation. It is known from experimental data that for the transformation of K-
577 feldspar into buddingtonite, X_{NH_4} in the fluid must be very high (Pöter et al., 2004).

578 Laser-ablation dating with the $^{39}\text{Ar}/^{40}\text{Ar}$ method of the muscovite from the breccia yielded an
579 age of 1491 ± 9 Ma (MSWD 0.98), interpreted as the age of the hydrothermal breccia formation
580 (Franz et al., 2021). Analyses of buddingtonite yielded an age range from 383 ± 12 Ma to 563 ± 14
581 Ma, and the oldest age of 563 Ma is interpreted as a minimum age, because of probable Ar-loss
582 of the very fine-grained buddingtonite crystals. This minimum age is in the same range as the
583 results of our attempt to date the fossils directly with Pb-Pb-dating (Fig. 14). The maximum
584 age is given by the intrusion age of the pegmatites, 1760 ± 3 Ma (Fig. 1; Shumlyanskyy et al.,
585 2021). The intrusion depth of 2 to 2.5 km might have been the depth for the microbial
586 community, but there is a significant time lag between pegmatite formation (1.76 Ga) and the
587 formation of the breccia (c. 1.49 Ga) during which exhumation could have occurred.

588 Silicification of microbial organisms is typical for geyser systems, as shown by many recent
589 analogues, e.g. for Yellowstone, USA (Cady and Farmer, 1996), Waiotapu, New Zealand
590 (Handley et al., 2008) and others (see references in Alleon et al, 2016). Consequently, a number
591 of experimental studies on silicification of microorganisms including the processes of silica
592 polymerization and precipitation in the presence of microorganisms was undertaken, starting
593 with the earliest work by Oehler (1976). Experimental silicification of archaea (Orange et al.,
594 2009) has shown that the outer surface layer of these organisms is the site for incipient
595 silicification, and the ubiquity of biofilms on surfaces in hot-springs (e.g. Cady and Farmer,
596 1996; Handley et al., 2008; Kremer et al., 2012) and other environments (Bortnikov et al., 2012)
597 indicates potential presence of biofilms also in the Precambrian at the subvolcanic geyser
598 system in the Korosten pluton. Extracellular polymeric substances play an important role in
599 silicification and fossilization as shown by many authors (see references above, and therein),
600 and fossilization of biofilms occurs very rapidly (Rozanov, 2003). After silicification of
601 extracellular polymeric substances, clay minerals developed on the surface of the fossils from
602 Volyn. This phenomenon was also observed in experimental studies (Urrutia and Beveridge,
603 1994) and in natural environments (Kremer et al., 2012; Bortnikov et al., 2012).

604 The formation of the 1-2 μm thick layer of Si-Al infiltration and development of encrustations
605 of Al-silicates was essential for the excellent preservation of the morphology of the
606 microfossils. The fossilization of organisms without skeletal parts requires special conditions,
607 which prevent autolysis. In fossilization experiments of crustacean eggs with phosphoric acid,
608 Hippler et al. (2012) pointed out that rapid heating before treatment with phosphoric acid was
609 essential for perfect preservation of the morphology of OM. This treatment denaturalized the
610 proteins of the crustacean eggs, creating a stable template for mineralization, which occurred
611 rapidly within one to two weeks. We suspect a similar process for the silicification process at
612 the Volyn locality. Anoxic conditions in the deep biosphere prevented early autolysis of the
613 organisms, then shock heating might have occurred due to influx of hot hydrothermal waters

614 into the miarolitic caves, carrying SiF_4 together with Al, Ca, and other elements, producing
615 rapid infiltration of Si, Al, and Ca into the outer surface layer of the organisms, including
616 precipitation of opal (Fig. 4f). The early envelope of silicification minimizes the molecular
617 degradation of the fossils, as also shown experimentally by Alleon et al. (2016). Further heating
618 (without deformation) after formation of the Si-Al enriched outer rim enhanced the decay, but
619 did not destroy the morphology. Kremer et al. (2012) pointed out that the morphology of
620 calcified cyanobacteria was destroyed, whereas silicification, when rapid, helps to preserve
621 their morphological details (e.g., Bartley, 1996; Manning-Berg et al., 2019, and references
622 therein). That fossilization of bacterial organisms is a rapid process has also been postulated by
623 Rozanov (2003). Raff et al. (2008) demonstrated experimentally that under anoxic conditions
624 (preventing autolysis) rapid formation of bacterially induced biofilms on the surface of
625 organisms provided the site for early mineralization with Ca-minerals. These biofilm bacteria
626 induce a catalyzing process for rapid fine-grained mineralization, which was also postulated by
627 Briggs (2003). Extracellular polymeric substances are known to provoke diagenetic
628 mineralization, possibly as the result of liberation of adsorbed cations during degradation (Arp
629 et al., 1999; Dupraz and Visscher, 2005; Altermann et al., 2006). Notably, most of the cases
630 described in the literature and quoted above deal with marine environments, whereas the case
631 reported here deals with a Precambrian continental, subsurface environment. Only in the
632 continental environment fluids rich in F are present; in the oceanic environment granites are
633 much less abundant than mafic rocks and they commonly lack F-enriched pegmatites.

634 Extracellular biosilicification capability of bacteria and archaea in geothermal environments
635 with transformation of soluble $\text{Si}(\text{OH})_4$ into nano-scale SiO_2 precipitates on the surface has
636 recently been emphasized by Ikeda (2021). Bacteria, such as *Thermus thermophilus* (Iwai et
637 al., 2010), can form siliceous deposits from supersaturated solutions in biofilms on the outer
638 surface layer of the cell envelope.

639 Zhmur (2003), based on the data by Gorlenko et al. (2000) and by comparison with other
640 occurrences in igneous rocks and in recent geyser environments, proposed a hydrothermal
641 origin of cyanobacteria and microbial bio-mats in geyser ponds for the Volyn occurrence. The
642 fossilization occurred in situ in zones of silica precipitation, forming sealed cup-like structures.
643 The floating cyanobacterial mat was buried in the self-sealed biogenic-geyser structure that was
644 formed at the hydrothermal discharge site, and collapse of these structures produced the breccia,
645 observed at the Volyn deposit. This model implies that the fossils were transported downward
646 with the geyser water to the chambers, because photosynthesizing cyanobacteria must have
647 lived at the surface. This is not consistent with our observations, which show that the filaments,
648 together with irregular and spherical kerite grew onto and into the etch pits of beryl (Fig. 3a).
649 If transport had occurred, this would have probably destroyed the delicate filaments, producing
650 a mat-like OM, such as described by Zhmur (2003).

651

652 **4 Concluding remarks**

653 The pegmatitic Volyn kerite occurrence is probably one of the localities world-wide with the
654 best preserved Precambrian microfossils. Common occurrences of (Precambrian) fossils are in
655 sedimentary rocks, especially in chert, but there is growing evidence of OM in the pore space
656 of igneous rocks (Ivarsson et al., 2020). Several factors have contributed to the micro-
657 taphonomical process to preserve the Volyn fossils as part of an endolithic micro-ecosystem.
658 First, the chambers in the pegmatites provided an exceptionally large 'pore' space. Secondly,
659 water was present in such an environment, necessary for life, although this space was not
660 necessarily completely water-filled, but possibly a cavity with temporary changes in the water
661 level. Transport of Si was likely enhanced by F, present in this pegmatitic, granitic environment.
662 OM would have decayed, when O was available, hence silicification of the outer parts of the
663 kerite fossils implies rapid reaction with Si and shielding for access of O. This environment in

664 the deep biosphere was similar to geyser systems, which are known to be sites of preferred
665 microbial growth. The microorganisms contribute to the microstructural development of
666 geysers by providing a favored substrate for opaline silica precipitation, and encrustation and
667 degradation of microorganisms is the dominant mode of fossilization at the high temperature
668 end of the geyser system (Cady and Farmer, 1996).

669 There is growing awareness of the importance of life in the deep igneous biosphere especially
670 in the record of early life, the most important reservoir of biomass in the Precambrian (Ivarsson
671 et al. 2020). The presence of F-rich hydrothermal waters in the late stage of granitic,
672 subvolcanic plutons might be a common scenario for preservation of microorganisms, without
673 the later influence of deformation and metamorphism, such as in chert, where most of the
674 studies of Precambrian fossils has been undertaken. Granitic rocks might be sites for the very
675 early diagenetic emplacement of silica, leading to 3D preservation of non-biomineralizing
676 fossils, the “Bitter Springs-type preservation” (Butterfield, 2003). The search for indications
677 for early life, and its evolution during the Precambrian has concentrated mainly on submarine
678 hydrothermal vents (e.g. Dodd et al., 2017), but it should be extended also to terrestrial
679 environments.

680

681 **Acknowledgements**

682 We thank A. Schreiber for preparation of FIB foils and D. Hippler for comments on an earlier
683 version, two anonymous reviewers for their careful and helpful reviews, and Tina Treude for
684 editorial handling.

685 **Author contributions:** GF (concept, writing), PL (sampling, reviewing), VC (sampling), VK
686 (sampling), H-MS (reviewing, reflected light microscopy), NM (pyrolysis), RW (TEM), JG (U-
687 Th-Pb), UG (SEM), JN (EMPA)

688 **Funding:** VK acknowledges financial support from Akademisches Auslandsamt Technische
689 Universität Berlin.

690

691 **References**

692 Alleon, J., Bernard, S., Le Guillou, C., Daval, D., Skouri-Panet, F., Pont, S., Delbes., and
693 Robert, F.: Early entombment within silica minimizes the molecular degradation of
694 microorganisms during advanced diagenesis, *Chem. Geol.*, 437, 98-108, 2016.

695 Altermann, W., Kazmierczak, J., Oren, A., and Wright, D. T.: Cyanobacterial calcification and
696 its rock-building potential during 3.5 billion years of Earth history, *Geobiology*, 4,147–166,
697 2006.

698 Arp, G., Reimer, A., Reitner, J.: Calcification in cyanobacterial biofilms of alkaline salt lakes,
699 *Eur. J. Phycol.*, 34, 393–403, 1999.

700 Bartley, J. K.: Actualistic taphonomy of cyanobacteria: implications for the Precambrian fossil
701 record, *Palaios*, 571-586, 1996.

702 Burnham, A.K., and Sweeney, J.J.: A chemical kinetic model of vitrinite maturation and
703 reflectance, *Geochim. Cosmochim. Acta*, 53, 2649-2657, 1989.

704 Butterfield, N. J.: Exceptional fossil preservation and the Cambrian explosion, *Integr. Compar.
705 Biol.*, 43, 166-177, 2003.

706 Bobos, I., and Williams, L. B.: Boron, lithium and nitrogen isotope geochemistry of NH₄-illite
707 clays in the fossil hydrothermal system of Harghita Băi, East Carpathians, Romania, *Chem.
708 Geol.*, 473, 22-39, 2017.

709 Bortnikov, N. S., Novikov, V. M., Soboleva, S. V., Savko, A. D., Boeva, N. M., Zhegallo, E.
710 A., and Bushueva, E. B.: The role of organic matter in the formation of fireproof clay of the
711 Latnenskoe Deposit, *Dokl. Earth Sci.*, 444, No. 1, 634-639, 2012.

712 Briggs, D. E. G.: The role of decay and mineralization in the preservation of soft-bodied fossils,
713 *Annu. Rev. Earth Planet. Sci.*, 31, 275–301, 2003.

714 Cady, S. L., and Farmer, J. D.: Fossilization processes in siliceous thermal springs: trends in
715 preservation along thermal gradients, *Evolution of hydrothermal ecosystems on Earth and
716 Mars? Chichester (Ciba Foundation Symposium)*, Wiley, 202, 150-173, 1996.

717 Dodd, M. S., Papineau, D., Grenne, T., Slack, J. F., Rittner, M., Pirajno, F., O'Neill, J., and
718 Little, C. T.: Evidence for early life in Earth's oldest hydrothermal vent precipitates, *Nature*,
719 543(7643), 60-64, 2017.

720 Dormans H.N.M., Huntgens F.J. and van Krevelen D.W.: Chemical structure and properties
721 of coal: 20. Composition of the individual macerals, *Fuel* 36, 321-339, 1957.

722 Dupraz, C., Visscher, P. T.: Microbial lithification in marine stromatolites and hypersaline
723 mats, *Trends Microbiol.* 13, 429–438, 2005.

724 England, W., and Mackenzie, A.: Some aspects of the organic geochemistry of petroleum
725 fluids, *Geolog. Rundschau* 78, 291-30, 1989.

726 Franz, G., V. Khomenko, Vishnyevskyy, A., Wirth, R., Struck, U., Nissen, J., Gernert, U., and
727 Rocholl, A.: Biologically mediated crystallization of buddingtonite in the Paleoproterozoic:
728 Organic-igneous interactions from the Volyn pegmatite, Ukraine, *Amer. Mineral.*, 10, 2119-
729 2135, 2017.

730 Franz, G., Sudo, M., Khomenko, V.: ⁴⁰Ar/³⁹Ar dating of a hydrothermal pegmatitic
731 buddingtonite-muscovite assemblage from Volyn, Ukraine, *Eur. J. Mineral.*, 34, 7-21, 2021.

- 732 Ginzburg, A.I., Bulgakov, V.S., Vasilishin, I.S., Luk'yanova, V.T., Solntseva, L.S., Urmenova,
733 A.M., and Uspenskaya, V.A.: Kerite from pegmatites of Volyn, Dokl. Akad. Nauk SSSR, 292,
734 188–191, 1987, (in Russian).
- 735 Gorlenko, V.M., Zhmur, S.I., Duda, V.I., Osipov, G.A., Suzina, N.E., and Dmitriev, V. V.: Fine
736 structure of fossilized bacteria in Volyn kerite, Origin of Life and Evolution of the Biosphere,
737 30, 567–577, 2000.
- 738 Handley, K. M., Turner, S. J., Campbell, K. A., and Mountain, B. W.: Silicifying biofilm
739 exopolymers on a hot-spring microstromatolite: templating nanometer-thick laminae,
740 Astrobiol., 8(4), 747-770, 2008.
- 741 Hippler, D., Hu, N., Steiner, M., Scholtz, G., and Franz, G.: Experimental mineralization of
742 crustacean eggs: new implications for the fossilization of Precambrian–Cambrian embryos,
743 Biogeosci., 9(5), 1765-1775, 2012.
- 744 Horsfield, B.: Practical criteria for classifying kerogens: Some observations from pyrolysis-gas
745 chromatography, Geochim. Cosmochim. Acta, 53, 891-901, 1989.
- 746 Ikeda, T.: Bacterial biosilicification: a new insight into the global silicon cycle, Biosci.,
747 Biotechn., Biochem., 85, 6, 1324-1331, 2021.
- 748 Ivanovich, P. V., and Alekseevich, D. S.: Mineralogy of the Volynian chamber pegmatites,
749 EKOST Association, Mineral. Almanac, 12, 128 p, Moscow, 2007.
- 750 Ivarsson, M., Drake, H., Neubeck, A., Sallstedt, T., Bengtson, S., Roberts, N. M. W., and
751 Rasmussen, B.: The fossil record of igneous rocks, Earth Sci. Rev., 210, 2020.
- 752 Iwai, S., Doi, K., Fujino, Y., Nakazono, T., Fukuda, K., Motomura, Y., and Ogata, S.: Silica
753 deposition and phenotypic changes to *Thermus thermophilus* cultivated in the presence of
754 supersaturated silica, The ISME J. 4, 809–816, 2021.
- 755 Kalyuzhnyi V. A., Voznyak, D. K., Gigashvili, G. M.: Mineral-forming fluids and mineral
756 paragenesis of chamber pegmatites of Ukraine, Kyiv: Naukova Dumka, 216 pp., 1971 (in
757 Ukrainian).
- 758 Kremer, B., Kazmierczak, J., Lukomska-Kowalczyk, M., and Kempe, S.: Calcification and
759 silicification: fossilization potential of cyanobacteria from stromatolites of Niuafu'ou's Caldera
760 Lakes (Tonga) and implications for the early fossil record, Astrobiol. 12(6), 535-548, 2012.
- 761 Larter, S.R.: Application of analytical pyrolysis techniques to kerogen characterisation and
762 fossil fuel exploration/exploitation, in: Voorhees, K. (Ed.): Analytical pyrolysis, methods and
763 applications. Butterworth, London, pp. 212-275, 1984.
- 764 Lukashev, A. N.: Depth of pegmatite formation, Moscow, Nedra, 152 pp., 1976, (in Russian).
- 765 Lu'kyanova, V. T., Lobzova, R. V., and Popov, V. T.: Filaceous kerite in pegmatites of Volyn,
766 Izvest. Ross. Akad. Nauk Ser. Geologicheskaya, 5, 102–118, 1992 (in Russian).
- 767 Lyckberg, P., Chernousenko, V., and Wilson, W. E.: Famous mineral localities: Volodarsk-
768 Volynski, Zhitomir Oblast, Ukraine, The Mineral. Record 40, 473-506, 2009.
- 769 Lyckberg, P., Chournousenko, V., and Chournousenko, O.: Giant heliodor and topaz pockets
770 of the Volodarsk chamber pegmatites, Korosten pluton, Ukraine, 36th Intern. Gemm. Conf..
771 Nantes, France, Abstr. vol., 78-83, 2019.
- 772 Mahlstedt, N., di Primio, R., and Horsfield, B.: On the shale gas potential of the Georgina Basin,
773 Record 2014 Geoscience Australia, Canberra, 2014.

774 Mahlstedt, N., di Primio, R., Horsfield, B., and Boreham, C.J.: Multi-component kinetics and
775 late gas potential of selected Cooper Basin source rocks, *Record 2015/19 Geosci. Australia*,
776 Canberra, pp. 199. <http://dx.doi.org/10.11636/Record.12015.11019>, 2015.

777 Manning-Berg, A. R., Wood, R. S., Williford, K. H., Czaja, A. D., and Kah, L. C.: The
778 taphonomy of proterozoic microbial mats and implications for early diagenetic silicification,
779 *Geosci.*, 9, 40, 2019.

780 Oberlin A., Boulmier J.L., and Durand B.: Electron microscope investigation of the structure
781 of naturally and artificially metamorphosed kerogen, *Geochim. Cosmochim. Acta*, 38, 647-650,
782 1974.

783 Oehler, J.H.: Experimental studies in Precambrian paleontology: structural and chemical
784 changes in blue-green algae during simulated fossilization in synthetic chert, *Geol. Soc. Am.*
785 *Bull.* 87 (1), 117–129, 1976.

786 Orange, F., Westall, F., Disnar, J. R., Prieur, D., Bienvenu, N., Le Romancer, M., and Défarge,
787 C.: Experimental silicification of the extremophilic Archaea *Pyrococcus abyssi* and
788 *Methanocaldococcus jannaschii*: applications in the search for evidence of life in early Earth
789 and extraterrestrial rocks, *Geobiol.*, 7(4), 403-418, 2009.

790 Pöter, B., Gottschalk, M., and Heinrich, W.: Experimental determination of ammonium
791 partitioning among muscovite, K-feldspar, and aqueous chloride solutions, *Lithos*, 74, 67–90,
792 2004.

793 Poetz, S., Horsfield, B., and Wilkes, H.: Maturity-driven generation and transformation of
794 acidic compounds in the organic-rich Posidonia Shale as revealed by electrospray ionization
795 Fourier transform ion cyclotron resonance mass spectrometry, *Energy Fuels*, 28, 4877–4888,
796 2014.

797 Quigley, T. M., and Mackenzie, A. S.: The temperatures of oil and gas formation in the sub-
798 surface, *Nature*, 333, 549-552, 1988.

799 Radke M., Horsfield B., Littke R. and Rullkötter, J.: Maturation and petroleum generation. In:
800 Welte, D.H., Horsfield, B., Baker, D.R. (Eds.), *Petroleum and Basin Evolution: Insights from*
801 *Petroleum Geochemistry, Geology and Basin Modeling*. Springer Berlin Heidelberg, Berlin,
802 Heidelberg, 169–229, 1997.

803 Raff, E. C., Schollaert, K. L., Nelson, D. E., Donoghue, P. C., Thomas, C. W., Turner, F. R.,
804 and Raff, R. A.: Embryo fossilization is a biological process mediated by microbial biofilms,
805 *Proc. Nat. Acad. Sci.*, 105(49), 19360-19365, 2008.

806 Rozanov, A. Yu.: Fossil bacteria, sedimentogenesis, and the early biospheric evolution,
807 *Paleontol. Zh.*, No. 6, 41–49, 2003, [*Paleontol. J.* 37 (6), 600–608 (2003)].

808 Shumlyanskyy, L., Belousoca, E., and Petrenko, O.: Geochemistry of zircons from basic rocks
809 of the Korosten anorthosite-mangerite-charnockite-granite complex, northwestern region of the
810 Ukrainian Shield, *Mineral. Petrol.*, 111(4), 459-466, 2017.

811 Shumlyanskyy, L., Franz, G., Glynn, S., Mytrokhyn, O., Voznyak, D., and Bilan O.:
812 Geochronology of granites of the western part of the Korosten AMCG complex (Ukrainian
813 Shield): implications for the emplacement history and origin of miarolitic pegmatites, *Eur. J.*
814 *Min.*, 33, 703-716, 2021.

815 Sinninghe Damsté, J.S., Eglinton, T.I., De Leeuw, and J.W., Schenck, P.A.: Organic sulphur in
816 macromolecular sedimentary organic matter: I. Structure and origin of sulphur-containing
817 moieties in kerogen, asphaltenes and coal as revealed by flash pyrolysis, *Geochim. Cosmochim.*
818 *Acta*, 53, 873-889, 1989.

- 819 Tahán, J. E., Granadillo, V. A., Sánchez, J. M., Cubillán, H. S., and Romero, R. A.:
820 Mineralization of biological materials prior to determination of total mercury by cold vapour
821 atomic absorption spectrometry, *J. Anal. Atomic Spec.*, 8(7), 1005-1010, 1993.
- 822 Urrutia, M. M., and Beveridge, T. J.: Formation of fine-grained metal and silicate precipitates
823 on a bacterial surface (*Bacillus subtilis*), *Chem. Geol.*, 116(3-4), 261-280, 1994.
- 824 Tissot, B.P., and Welte, D.H.: Petroleum formation and occurrence, 2nd ed. Springer-Verlag,
825 Berlin, 1984.
- 826 Vermeesch, P.: IsoplotR: a free and open toolbox for geochronology, *Geosci. Front.*, 9, 1479-
827 1493, 2018 doi: 10.1016/j.gsf.2018.04.001.
- 828 Voznyak, D.K., Khomenko, V.M., Franz, G., and Wiedenbeck, M. Physico-chemical
829 conditions of the late stage of Volyn pegmatite evolution: Fluid inclusions in beryl studied by
830 thermobarometry and IR-spectroscopy methods, *Mineral. J. (Ukraine)*, 34, 26–38, 2012 (in
831 Ukrainian).
- 832 Wirth, R.: Focused Ion Beam (FIB): a novel technology for advanced application of micro-and
833 nanoanalysis in geosciences and applied mineralogy, *Eur. J. Mineral.*, 16, 863–876, 2004.
- 834 Wirth, R.: Focused ion beam (FIB) combined with SEM and TEM: Advanced analytical tools
835 for studies of chemical composition, microstructure and crystal structure in geomaterials on a
836 nanometre scale, *Chem. Geol.*, 261, 217-229, 2009.
- 837 Zhmur, S. I.: Origin of Cambrian fibrous kerites of the Volyn region, *Lithol. Mineral Resour.*,
838 38, 55-73, 2003.